OXIDATION AND PHOTOOXIDATION OF SINGLE-CRYSTAL $BiI_3(001)$ SURFACES IN AQUEOUS OR OXYGEN ENVIRONMENTS

WPI

Roy Stoflet
In partial requirements for the
Degree of Masters of Science, M.S. in Chemistry
submitted to the Faculty of
WORCESTER POLYTECHNIC INSTITUTE
100 Institute Road, Worcester, Massachusetts 01609

Committee: Professors Patricia Z. Musacchio (CBC, chair),
Pratap M. Rao (Mech. E.), and Ronald L. Grimm (CBC, advisor)

CONTENTS

LIST OF FIGURES

LIST OF TABLES

PREFACE

BiI_3 is a non-toxic solar absorber material that is well matched for tandem-junction photovoltaic devices. We synthesized single-crystal samples via chemical vapor transport and physical vapor transport in evacuated ampoules to yield BiI_3 flakes with mm^2-to-cm^2 terraces and explored the effect of various oxidizing atmospheres. Oxidation methods included immersion in degassed water, ultraviolet illumination under an oxygen ambient, and a sequence of ultraviolet illumination under oxygen and subsequent water immersion. X-ray photoelectron spectroscopy (XPS) and X-ray diffraction (XRD) quantified the chemical changes as a function of oxidative treatments. Spectra reveal that water immersion of BiI_3 yields BiOI(102) reflections that are thicker than photoelectron probe depths. Ultraviolet illumination under an oxygen ambient forms bismuth oxide that subsequently converts to BiOI(001) upon water immersion. We discuss the implications of these surface chemical transformations for the long-term atmospheric stability of BiI_3-containing solar energy conversion devices.

ACKNOWLEDGMENTS

Above all, I would like to thank my amazing wife Angela for her unyielding support and unending patience as she was left home alone while I worked nights and weekends in the lab. Absolutely none of this would be possible without her.

For recent inspiration, I would like to thank a small group of faculty and students at WPI who had a major impact on me. Alex and Julia who both mentored me and managed to not show their disdain as I vented the XPS multiple times. Curtis and Kat who both were very helpful in conducting experiments. Special thanks go to Patti Musacchio and Pratap Rao for being friends as well as committee members for my Defense. And Anita Mattson for helping me find the correct path to where I am now. And although he demurs from any such notoriety, my deepest thanks go to Ron Grimm for giving a late-thirties engineer a chance to tinker in the lab.

As for the foundations of my desire for higher learning, there is simply a staggering list of family and friends who have helped me along the way. However, I would like to take a moment to name a few of them specifically for their profound impact on my career and my passions. To R. Chuck Schubert, who is not only my uncle and good friend but also the first person my family

to receive a college degree, you were a beacon showing the way along the trail that you were the first in our family to blaze. To Bob Papile, thank you for convincing me that I was capable of more than I thought possible at the time. And finally, to those who have mentored me and believe in me during my career, Mike Loughnane, Buddy Colmery, and Alan Huber stand out as particular inspirations.

R. S., April 2022

GLOSSARY

CVD	Chemical vapor deposition
fwhm	Full-width at half-maximum
ppm	Parts per million
PV	Photovoltaic(s)
PVD	Physical vapor deposition
pXRD	Powder X-ray diffraction (technique) *or* powder X-ray diffractometer (instrument)
SF	Sensitivity Factor
UV	Ultraviolet
XPS	X-ray photoelectron spectra *or* X-ray photoelectron spectroscopy (technique) *or* X-ray photoelectron spectrometer (instrument)

XRD	X-ray diffraction (technique) *or* X-ray diffractometer (instrument)

SYMBOLS

$\mathbf{E}_g$	band gap
f_G	Gaussian full-width at half-maximum
f_L	Lorentzian full-width at half-maximum
f_V	Voigt full-width at half-maximum

CHAPTER 1

INTRODUCTION

As the climate and environmental impact of fossil fuel consumption becomes more evident, creative means of harvesting energy from more environmentally sustainable sources increases in importance.[1] Among viable renewable energy sources available, photovoltaic energy conversion remains one of the most promising.[2] The focus of intense research into solar energy conversion has fueled an impressive increase in the energy efficiency of this technology with a present focus on tandem-junction devices both from similar lattice-matched and from dissimilar materials.[3] Unfortunately, the majority of lattice-matched materials are highly expensive. Other inexpensive yet highly efficient materials of recent interest contain biologically harmful materials such as heavy metals such as Cd and Pb that pose health hazards for installation workers and include high risks of deleterious environmental impacts as the devices break down.[4–5] The challenge of finding environmentally friendly, inexpensive, and non-toxic solar absorbers drives research into straightforwardly synthesized, underexplored materials with band gap energies that might complement silicon in a tandem-junction solar absorber.

Among non-toxic alternatives to the heavy-metal-containing perovskites that currently dominate the high efficiency dual junction solar field, researchers consider bismuth triiodide (BiI_3) as a top-absorber-candidate material.[6–9] The bulk of energy-conversion research with BiI_3 has included room-temperature gamma ray[10–14] and X-ray detection material,[15–18] but recent applications have extended to solar energy,[19–20] and particularly to hole-transport layers for organic solar cells.[21–22] Reports on BiI_3 indicate an indirect band gap[23] with energy values between 1.67–1.82 eV,[24–26] which represents an ideal range for an absorber material to serve as the top junction in a tandem-junction absorber configuration.[27]

Motivated by the non-toxicity and favorable band gap energy of BiI_3, researchers have synthesized BiI_3 and probed its solar energy performance. BiI_3 may be synthesized from inexpensive precursors to yield nanoplates,[28–30] nanotubes,[31–32] vertically oriented nanoflake films,[33] and single crystals[34–36] based on growth method or deposition substrate. In recent years BiI_3-based devices have demonstrated significant improvements in performance in photovoltaic applications including one experiment which yielded a short-circuit current density of 12.6 mA cm^{-2},[23] and a separate study utilized iodization of BiSI to achieve a 1.33% power conversion efficiency with a fill factor of ~40% and an open-circuit voltage exceeding 600 mV.[37] Despite promising results for solar energy conversion, BiI_3 appears to suffer from reduced performance from crystalline defects as well as issues relating to long-term instability under exposure to ambient environments.[38] While research has addressed the atmospheric stability of other non-traditional solar absorber materials,[39] few studies have explored the environmental and oxidative stability of BiI_3,[26,40] and questions remain regarding its degradation mechanisms as a function of specific oxidant. One report of BiI_3 thin films notes its oxidative breakdown in an air ambient in a reaction that may yield Bi_2O_3, but that manuscript did not focus on this oxidation reaction.[20] Conversely, in studies that quantify oxidation processes and products, the primary chemical reaction appears to be conversion to bismuth oxyiodide, BiOI, which some reports suggest it is actually beneficial to the carrier transport dynamics of devices constructed of BiI_3.[20,22] Literature reports highlight two independent reaction pathways for the transformation of BiI_3 to BiOI. Hydrolysis of BiI_3 in water to yield BiOI is documented in published literature dating back to the late 19th century.[41] Reports further present a second pathway, the decomposition of BiI_3 in pure oxygen, that only occurred at elevated temperatures.[42] Critically, few reports probe oxidation in BiI_3 that is facilitated both by chemical oxidants and by reactive free carriers resulting from above-band-gap illumination. Thus, significant knowledge gaps remain in the solar-PV-relevant atmospheric stability of BiI_3, and addressing such stability gaps motivates the present investigation.

Herein, we synthesize single-crystal BiI_3(001) via high-temperature, in vacuo chemical vapor transport, and characterize the interplay between chemical oxidants, above-bandgap illumination, and the subsequent interfacial chemical species. Oxidants include degassed water, a UV illumination under an oxygen ambient, and sequential exposures of O_2+UV and then water. For each treatment, X-ray photoelectron spectroscopy and X-ray diffraction respectively quantified the interfacial chemical speciation and the crystalline phases resulting from the oxidation process. The resulting processes and oxidative products yield a significantly more detailed picture of the stability and reactivity of BiI_3 materials relevant to energy conversion and detection devices.

CHAPTER 2

EXPERIMENTAL SECTION

2.1 Materials and Chemicals

All water requirements utilized 18 MΩ cm resistivity water from a Millipore Milli-Q system. Synthesis procedures for single-crystal bismuth iodide utilized either single-source BiI_3 (99%, Sigma-Aldrich, used as received), or a combination of elemental Bi (99.5%, Alfa Aesar, as received) and I_2 (99.99%Alfa Aesar, as received). Growth ampoules utilized quartz fused silica tubing (19 mm O.D., 1 mm wall, 4' long, Technical Glass Products, Inc., Painesville, Ohio). Quartz tube cleaning utilized NaOH (98.5%, Acros Organics). Prior to chemical loading, stock quartz tubes were cut to ~40 cm lengths, sealed at one end under an oxy-propane flame, and submerged in a 10 wt % $KOH_{(aq)}$ bath for at least one week. Following this base-bath submersion, tubes were rinsed copiously with water and stored in a >100 °C oven until use. Gases included oxygen (ultrahigh purity, Airgas) for oxidation studies, and argon (ultrahigh purity, Airgas) for sample drying and for degassing water.

2.2 Growth of Single-Crystal Bismuth Iodide

Physical-vapor deposition (PVD) or chemical-vapor deposition (CVD) yielded single-crystal bismuth iodide samples in sealed, evacuated quartz ampoules respectively from either single-source BiI_3, or from a combination of elemental bismuth and molecular iodine. Production of ampoules involved reagent loading and sealing as described previously.[43–44] Here, reagent loading totaled approximately 2.0 g of either BiI_3 for PVD or Bi+I_2 for CVD. CVD syntheses utilized a range of Bi:I ratios from 30% deficient to 36% excess of iodide relative to an ideal BiI_3 stoichiometric ratio. Qualitatively, CVD

growth with an iodine deficiency of approximately 15% consistently yielded large crystal growth and served as the source for all material under study. Each loaded tube was individually attached in a vertically oriented rotary evacuator, and the bottom of the tube with the reagents was submerged in an ice bath to lower the iodine vapor pressure for five minutes prior to evacuation. Connection to a diffusion-pump-equipped Schlenk line with a base pressure below 1×10^{-3} torr afforded evacuation of the test quartz test tube while sealing with an oxy+natural gas flame produced each evacuated ampoule.

Synthesis of BiI_3 within the evacuated, sealed ampoules proceeded in a two-zone tube furnace. A typical growth sequence followed an initial 1 °C min^{-1} temperature ramp and a 2 h soak with the reagent zone at 250 °C and a higher temperature of 330 °C in the deposition zone to clean out the deposition side of the ampoule. Growth proceeded during a 72 h soak step with the reagent zone at 330 °C and 250 °C in the deposition zone. We selected these temperatures based on reports of 0.1–1.0 torr $BiI_{3(g)}$ vapor pressures in this temperature range,[35] as well as remaining below both the 570 °C breakdown temperature of BiI_3 in inert environments,[45] and its >400 °C melting point. Such growth recipes yielded numerous mirror-like BiI_3 flakes with up to 1 cm^2 terraces in the deposition zone. Typical polycrystalline silver-to-orange remains in the reagent zone are likely a combination of BiI_3, BiOI, and possible Bi_2O_3 due to reaction with any trace oxygen remaining in an ampoule following sealing and are not analyzed herein.

2.3 Oxidative treatments

Mentioned above, we explored two pathways for oxidation of BiI_3 single crystals including immersion in degassed water. The selection of these two specific sets of treatments was initially guided by the work of other researchers utilizing similar conditions to probe the atmospheric stability of methylammonium lead triiodide perovskite materials for photovoltaic applications.[46] We additionally explored a third pathway involving sequential exposures to UV irradiation under an oxygen ambient followed by immersion in degassed water. For all oxidation reactions, flakes were cleaved immediately prior to treatment using double-sided consumer adhesive tape to provide a fresh surface for reactivity and analyses.

For the water-only oxidation pathway, we immersed single-crystal BiI_3 samples in degassed water immediately after cleaving. Degassing involved sparging with argon for 20 min prior to use as well as maintaining a positive argon flow for the duration of water exposures. Water immersion durations at ambient temperature ranged from 10 to 90 min. Following water exposure, samples were dried under argon and directly analyzed via XRD

or stored until XP spectroscopy in a recirculating glovebox with an oxygen partial pressure below 1 ppm as measured at a commercial oxygen sensor.

For the oxidation pathway utilizing a sequential O_2+UV and subsequent water exposure, freshly cleaved single BiI_3 crystals were first sealed in a vacuum-flask. The flask was then evacuated on a Schlenk line and backfilled with pure oxygen to a pressure slightly above the ambient atmosphere. Under the oxygen ambient, the sample was placed for 48 h under illumination from a 36 W, 395 nm consumer LED lamp that delivered an irradiance of 90 ± 9 mW cm^{-2} as measured at a silicon photodiode (FDS100, Thorlabs). Following the 48 h UV exposure, the sample was removed from the flask and immersed in argon-sparged water as above. Samples were immersed for times ranging from ten to ninety minutes to match exposure conditions for the water-only oxidation. Following water exposure, samples were dried under argon and directly analyzed or stored in a recirculating glovebox until analysis.

2.4 X-ray Diffraction

Diffraction experiments utilized a Bruker D8 Advance powder X-Ray diffractometer with Bragg-Bentano geometry and Cu Kα radiation. Double-sided tape affixed individual flakes to amorphous glass slides. Scans were conducted for each sample over the 5–42° angular range at 0.01° steps and a two-second dwell time per increment.

For the products of BiI_3 oxidation, the Scherrer equation yielded an estimated crystallite size from the Gaussian component of each peak.[47] While the default value of 0.9 for K is common, Garg et al. uses a value of 0.94 specifically for analysis of BiI_3 that we employ herein.[46] A LabVIEW-based, in-house-developed, peak-fitting program fit pseudo-Voigt peak shapes to 2:1 area doublets as appropriate for the Cu Kα radiation. Equation 2.1 subsequently deconvolved the Gaussian contribution to peak width, f_G, due to crystallite particle size from the Lorentzian-shaped instrumental-line-broadening widths, f_L, based on interpreting experimentally quantified fwhm values as pseudo-Voigt peak widths, f_V.[49]

$$f_V \approx 0.5346 f_L + \sqrt{0.2166 f_L^2 + f_G^2} \tag{2.1}$$

We determined Lorentzian-shaped instrumental-line-broadening widths, f_L, based on the width of the (003), (006), (009), etc. features in an XRD trace of a freshly cleaved BiI_3 single crystal sample. For the freshly cleaved single-crystal sample, a fit of the (003) reflection at $2\theta = 12.9°$ revealed a fwhm of 0.0351°, while fwhm values of 0.0373° and 0.0412° well fit the (006) and (009) features, respectively. A quadratic extrapolation of the single-crystal fwhm values established eq 2.2 throughout the 2θ range under consideration.

$$f_L = 0.034613^\circ + -2.6205 \times 10^{-5}(2\theta) + 4.9577 \times 10^{-6}(2\theta)^2(1^\circ)^{-1} \qquad (2.2)$$

2.5 Photoelectron Spectroscopy

A Physical Electronics (Phi) 5600 system with a third-party data acquisition system (RBD Instruments, Bend, Oregon) analyzed surface states and stoichiometry as described previously.[43–44,50] Monochromatic Al Kα radiation was incident at 45° vs the sample surface and 90° relative to the take-off angle for detection. Peak quantification utilized an in-house-developed program[50] based on published spectral shapes[51] and corrected for instrument specific sensitivity factors,[52] and background energy loss functions. Background-energy-loss functions include a Shirley-type background,[53] or the integration of a Tougaard-style energy-loss function based on $B = 2900$ eV^2 and $C = 1643$ eV^2 within a universal function that is scaled to the height of the photoelectron data.[54–55] Pseudo-Voigt functions, GL(x), describe all spectral shapes as a non-linear product of Gaussian ($x = 0$) and Lorentzian ($x = 100$) functions. Throughout the presented results, fits to the Bi 4f region utilized GL(70) functions above a Shirley-type background, I $3d_{5/2}$ fits utilized GL(70) functions above a Tougaard background, and both C 1s and O 1s fitted features were well described by GL(30) functions above a Tougaard background. In the case of multiple fitted features within a particular chemical region, fits were constrained to have identical fwhm values.

Beyond the as-grown nascent samples and the chemical treatments described above, a vacuum cleaving process yielded one additional surface for comparison with the ambient results. Vacuum cleaving utilized an air-free transfer suitcase that mounts on the Phi 5600 load lock with a transfer arm that is aligned directly above a sample puck within the load lock chamber. For vacuum cleaving, the end of the suitcase transfer arm was coated with double-sided-adhesive carbon tape to align atop the BiI_3 sample on the analysis puck. Once the load lock and vacuum suitcase were evacuated to high vacuum under turbomolecular pumping, the suitcase transfer arm was lowered to apply the carbon tape to the BiI_3 sample, lifted off to reveal an in-vacuo-cleaved surface, and the sample was expeditiously transferred to the ultrahigh vacuum chamber for XP spectroscopy.

CHAPTER 3

RESULTS

3.1 X-Ray Diffraction

3.1.1 Oxidation via Water Immersion Only

Figure 3.1 displays representative XRD traces of freshly cleaved single-crystal BiI_3 subject immersions in degassed water for 10–90 min. Figure 3.1 presents the *y*-axis counts on a logarithmic scale to highlight small contributions from oxidation features that emerged during prolonged water immersions. Freshly cleaved (nascent) flakes with no water exposure as in Fig. 3.1A demonstrate sharp peaks at 13, 26, and 39° consistent with the (003), (006), and (009) faces of bismuth iodide. Immersion in degassed water for 10 min yields XRD features in Fig. 3.1B at 32° that is consistent with BiOI(110) reflections and a 29.7° reflection that reasonably corresponds to BiOI(003) or BiOI(102). Recalling that the BiOI unit cell contains one whole covalent layer in the c axis, the presence of a BiOI(003) reflection should further contain a reflection at 9.7° for BiOI(001) and 19.5° for BiOI(002). The lack of features at lower angles indicative of BiOI(001) or (002) suggests that the observed feature at 29.7° is a reflection from a (102) face rather than a (003) face. A 30 min immersion in degassed water as in Fig. 3.1C yields a more prominent reflection at 29.7° that we ascribe to the (102) face relative to the 10 min water immersion oxidation. Following immersion for 90 min, Fig. 3.1D reveals a BiOI(001)-ascribable feature at 9.7°. Considering the significantly larger fwhm for the 29.7° reflection as compared to the 9.7° reflection, we continue to ascribe the 29.7° reflection to a BiOI(102) face for samples subject to a 90 min oxidation in degassed water.

Interestingly, nearly all samples quantified by XRD including those in Fig. 3.1 demonstrated reflections at angles that are proportionally below the (003),

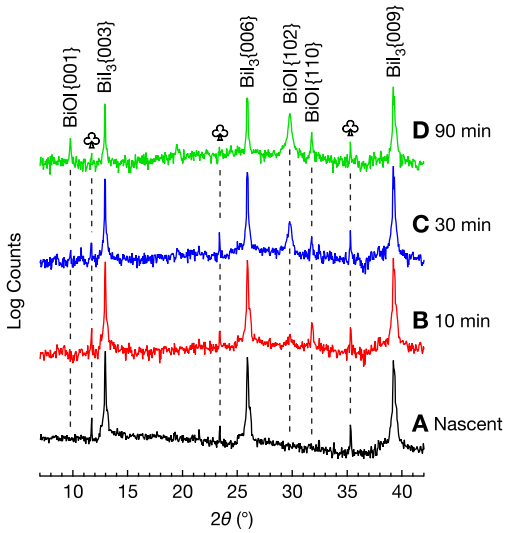

Figure 3.1 Sequential pXRD traces of freshly cleaved bismuth iodide flakes as a function of degassed water immersion time. Among features that appear with increasing water exposure, the BiOI(102) reflection dominates the oxidation features as compared to the (001) and (110) reflections. Features marked with club symbols, ♧, have 2θ reflection angles that scale with the (003), (006), (009) reflections, respectively.

(006), (009), etc. family that we denote with a ♧. These ♧-denoted features at 11.7, 23.4 and 25.3° are well described by reflections from BiI_3(003)-family faces but for a unit cell that is ~10.5% larger in the *c*-axis, or 2.285 nm in length rather than 2.067 nm. The minute intensities of ♧-denoted features relative to the primary (003), (006), and (009) reflections indicate that only a nominal number of unit cells that are affected by this phenomenon. A model that fits the data for a small fraction of unit cells that are expanded by ~0.2 nm includes the intercalation of molecular iodine during the iodine-mediated vapor-transport crystal growth. Such intercalation-driven shift in diffraction features is well precedented for 2-D layered materials.[56–57] With a present focus on interfacial oxidation rather than bulk chemistry and the small contribution of such features to the overall diffraction trace, the dynamics of such intercalation processes remain the subject of ongoing study.

3.1.2 Oxygen Pre-Treatment followed by Water Immersion

Figure 3.2 displays representative XRD traces of single-crystal BiI_3 subject to a 48-hour exposure to UV light excitation under an oxygen ambient followed by immersions degassed water for up to 90 min. As with Figure 3.1, Figure 3.2 presents the *y*-axis counts on a logarithmic scale to highlight small contributions from features that emerged due to oxidation. Flakes exposed to

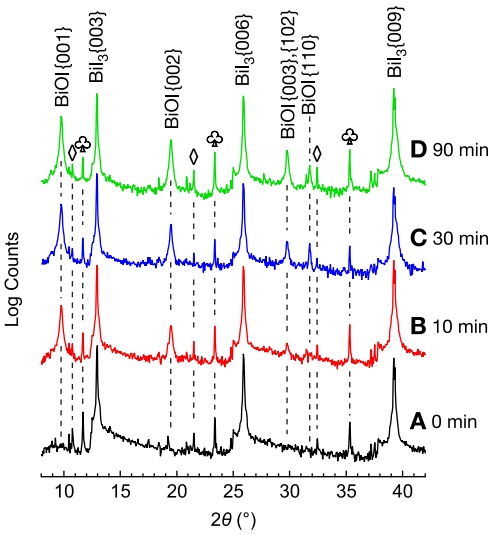

Figure 3.2 Sequential pXRD traces of freshly cleaved bismuth iodide flakes subjected to two days under UV irradiation in an oxygen ambient and subsequent water immersion for (A) 0 min, (B) 10 min, (C) 30 min, and (D) 90 minutes. Among oxidation-ascribable features that appear with increasing water exposure, the BiOI(001) reflection dominates the oxidation features as compared to the (110) reflection that is observed with the longer exposures. As with the traces in Fig. 3.1, features marked with club and diamond symbols, ♧ and ♢, have 2θ reflection angles that scale with the parent BiI_3(003), (006), (009) features.

UV illumination under oxygen with no subsequent water immersion as in trace A demonstrate sharp peaks at 13, 26, and 39° consistent with the (003), (006), and (009) faces of bismuth iodide. Immersion in degassed water for 10 min following the O_2+UV treatment yields XRD features in trace B at 9.7, 19.5, and 29.7° that are consistent with reflections from the (001), (002), and (003) faces of BiOI respectively. A 30-min immersion in degassed water following the O_2+UV treatment as in trace C yields more prominent reflection at 9.7, 19.5, and 29.7° relative to those in trace B. Further, the trace in Fig. 3.2C demonstrates the appearance of a feature at 32° that is consistent with a BiOI(110) reflection that is present in several traces in Fig. 3.1. Following a O_2+UV treatment and a 90-min water immersion, trace D shows increased intensity of each of the aforementioned oxidation-ascribed peaks but reveals no new features as compared to shorter immersion times. For each trace in Fig. 3.2B–D, the steadily decreasing amplitude from the 9.7 to the 19.5 to the 29.7° features and their mutually similar fwhm values together suggest that these arise from the same family of reflections, namely the (001), (002), and (003) of BiOI.

As with the traces in Fig. 3.1, the pXRD traces in Fig. 3.2 demonstrate families of reflections ascribable to larger *c*-axis unit cell sizes. Beyond the ♧-denoted features in Fig. 3.2 that align with the positions of ♧-denoted features in Fig 1, a set of ⋄-denoted features at 10.75, 21.5, and 32.4° well align with reflections from the (003), (006), and (009) planes if the *c*-axis unit cell length is 2.480 nm. An expansion to 2.480 nm represents a ~20% or 0.41 nm increase relative to the anticipated 2.0676 nm *c*-axis length. The observed features may also indicate a higher degree of intercalation in these samples. The traces presented in both Figs. 3.1 and 3.2 are representative, and it is important to note that a small fraction of pXRD traces acquired following a water immersion demonstrated features at the ⋄-denoted locations in Fig. 3.1. Specifically, small features at 21.5 and 32.4° in Fig. 3.1A likely correspond to the ⋄-denoted peaks present in the traces throughout Fig. 3.2. As with Fig. 3.1, the presentation of counts on a logarithmic *y* axis reinforces the minuscule contribution of these features to each overall spectrum that may be difficult to observe from non-single-crystal samples.

3.1.3 Scherrer Analysis for Grain Size

Table 3.1 presents the width values for the BiOI(102) feature at 29.7° shown in Fig. 3.2D that resulted from a 90 min treatment in degassed water; as well as for the BiOI(001), (002), and (003) family of reflections shown in Fig. 3.2D that resulted from exposure to UV under an oxygen ambient followed by a 90 min water exposure. Width values include the peak-fitted pseudo-Voigt f_V values from experimental data, angle-specific Lorentzian instrumental line-broadening contribution f_L, and the resulting Gaussian width values that should represent the contribution due to crystallite size, f_G. A Scherrer analysis yields the grain sizes for each f_G corresponding value. Table 3.1 lists fwhm values with excess significance that is truncated when presenting grain sizes.

Values provided in Table 3.1 describe the grain size for oxidative feature from two specific XRD traces, however these data are representative for the multiple samples under study. We interpret Scherrer-determined crystallite sizes in this context to be synonymous with layer thickness above a macroscopic 2-D material such as BiI_3. Thus, XRD results and the Scherrer analysis demonstrate that exposure of freshly cleaved BiI_3 to degassed water for 90 min predominantly yields ~50 nm of BiOI(102). In contrast to the water-only case, oxidation due to a sequential two-day UV exposure under an oxygen ambient followed by a 90-min immersion in water predominantly yields ~70 nm of BiOI(001) with smaller contributions from other facets such as BiOI(110). XRD-determined thickness values are valuable in the subsequent interpretation of photoelectron spectra, as oxidation feature thicknesses in the tens-of-nm greatly exceed typical photoelectron escape depths.

Table 3.1 Peak widths and the corresponding Scherrer-determined grain sizes for the major oxidation features observed in the XRD.[a]

Oxidation treatment		Component fwhm (°)			Grain
Feature	Centroid 2θ (°)	f_V	f_L	f_G	size (nm)
90 min water only					
BiOI(102)	29.7	0.2039	0.0382	0.1826	47
O_2+UV; 90 min water					
BiOI(001)	9.7	0.1295	0.0349	0.1100	76
BiOI(002)	19.5	0.1417	0.0360	0.1213	69
BiOI(003)	29.7	0.1476	0.0382	0.1259	68

3.2 X-Ray Photoelectron Spectroscopy

Figure 3.3 presents representative XP spectra for (A) vacuum-cleaved BiI_3(001) and spectra following oxidation treatments. Frames (B) and (C) present spectra following immersion in degassed water for 10 and 90 min respectively. Frames (D)–(F) contain spectra for samples that were subjected to a 48-h exposure to 395 nm, 90 ± 9 mW UV irradiation under an oxygen ambient with no subsequent water immersion as in frame (D), as well as subsequent water immersion for (E) 10 min, and (F) 90 minutes. For all samples under study, green-shaded I $3d_{5/2}$ features appear at 619.0–619.5 eV that is characteristic of iodide, and green-shaded Bi $4f_{7/2}$ features appear at 159.1–159.6 eV that implies interfacial Bi^{3+}. We ascribe red-shaded fitted features within the O 1s region with centers between 530.0–530.5 eV to contributions from metal-oxygen bonding.[50] Adventitious contamination likely yields the contributions of the blue-shaded fitted features in the O 1s and C 1s regions. Comparing peak binding-energy locations, the general alignment between all spectra in Fig. 3.3 demonstrates that the oxidation treatments do not significantly change oxidation states relative to the freshly cleaved sample in Fig. 3.3A. Following an assertion that oxidation will not remove interfacial bismuth but may deplete iodide and/or add oxygen,[26,41] Fig. 3.3 normalizes all regions for a given sample to the intensity of its Bi $4f_{7/2}$ feature.

While no oxidation state changes accompany changes in surface chemical species due to oxidation, changes in photoelectron peak areas are revealing. Vacuum-cleaved BiI_3(001) surfaces as in Fig. 3.3A yield expectedly strong Bi 4f and I 3d features with only trace adventitious carbon contaminants denoted with blue-shaded fitted features and no observable oxygen species within detection limits. As noted in Table 3.2, three vacuum-cleaved BiI_3 samples demonstrated a Bi:I ratio of 1:2.8 based on sensitivity-factor-corrected

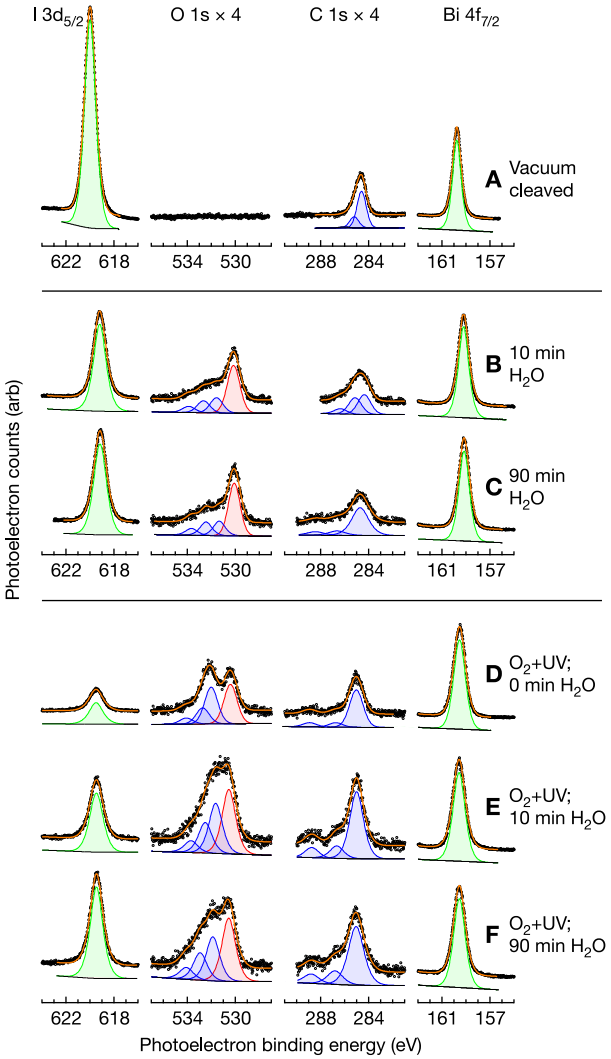

Figure 3.3 Representative XP spectra of (A) vacuum-cleaved $BiI_3(001)$; samples subjected to water immersion for (B) 10 min or (C) 90 min; and samples subjected to UV illumination under an oxygen ambient with (D) no subsequent water immersion, as well as with (E) 10 min and (F) 90 min of subsequent water immersion. Within the O 1s and C 1s regions we ascribe blue-shaded features to adventitious contaminants and the red-shaded O 1s feature to metallic oxides due to sample oxidation.

Table 3.2 Sensitivity-factor (SF) corrected XPS ratios for each oxidation treatment.[a]

Pretreatment	H_2O Immersion time (min)	Number of samples	SF-corrected peak areas		
			Bi ≡ 1	O	I
Vacuum Cleaved	*n/a*	3	1	<0.2	2.8
None	10	2	1	0.8	0.9
None	30	1	1	1	0.9
None	90	1	1	1	1.0
2 days O_2+UV	0	3	1	0.8	0.3
2 days O_2+UV	10	3	1	0.9	0.6
2 days O_2+UV	30	2	1	0.9	0.9
2 days O_2+UV	90	1	1	1.2	0.9

[a] All ratios are normalized to bismuth and represent averages from at least two samples.

photoelectron-peak-area ratios, which agrees well with the material's bulk stoichiometry. As one of the three vacuum-cleaved BiI_3 samples under study demonstrated trace O 1s features, Table 1 bounds the oxygen contribution to <0.2 for these otherwise pristine surfaces. For water-oxidized samples as in Fig. 3.3B–C, the O 1s region demonstrates metal-oxygen states in red as well as significantly suppressed I $3d_{5/2}$ areas relative to the vacuum-cleaved sample spectra in Fig. 3.3A. Interestingly, the Bi:O:I ratios in frames B and C strongly resemble each other, which is further reflected in the Table 3.2 values that demonstrate XPS-derived stoichiometries for Bi:O:I of nearly 1:1:1 for water-immersed samples. In concert with the XRD data above and with previous studies of BiOI from our group,[43] the XPS results support the presence of interfacial BiOI due to oxidation in water. The general similarity between Bi:O:I ratios throughout the water-immersion times in Table 3.2, and the similarity of spectra between frames B and C in Fig. 3.3 cumulatively suggest that water-driven oxidation yields layers of BiOI on BiI_3 that are thicker than the several-nm sampling depth in XPS even before the first 10 min of water immersion.

Oxidation due to a two-step treatment of UV irradiation in oxygen followed by water immersion demonstrates unique spectra relative to a one-step oxidation in degassed water. For the sample spectra in Figure 3D with only the O_2+UV treatment and no subsequent water immersion, the iodide peak area is significantly attenuated as compared both to the vacuum-cleaved sample spectra in Fig. 3.3A, as well as to spectra following water immersion as in Fig. 3.3B–C. Peak areas presented in Table 2 support a suppression of iodide with average Bi:O:I stoichiometries of 1:0.8:0.3 that may point to a thin film of interfacial oxide due to the O_2+UV treatment. Frames E and F from sam-

ples with a O_2+UV treatment and either 10 or 90 min in water show larger Bi-normalized I $3d_{5/2}$ peak areas as compared to a O_2+UV treatment and no water immersion. Interestingly, the Bi-normalized I $3d_{5/2}$ peak areas in Fig. 3.3E–F strongly resemble such I $3d_{5/2}$ peak areas in Fig. 3.3B–C that arise from only a water treatment. Table 3.2 further supports the relative changes in stoichiometries where the O_2+UV treatment with subsequent water immersion yielded Bi:O:I stoichiometries that vary somewhat but more closely resemble the 1:1:1 ratio observed following a water-only oxidation.

CHAPTER 4

DISCUSSION

The tendency of BiI_3 to oxidize under an air ambient to species including bismuth oxyiodide has been documented as far back as the nineteenth century.[41] Deeper elucidation of oxidation and photooxidation reactivity herein elucidates the presence of multiple oxidative mechanisms at play.

The cumulative diffraction and photoelectron spectroscopy data in Figs. 3.1–3.3 demonstrate that oxidation of BiI_3 follows reactant-dependent pathways. Comparing oxidation pathways, photoelectron spectroscopy reveals that water immersion quickly oxidizes nascent BiI_3(001) surfaces, and converts O_2+UV treated samples over a timescale of several minutes. X-ray diffraction, which has a significantly deeper probing distance than XPS, reveals increasing peak intensities of BiOI-ascribable features with prolonged water immersion. Despite changing XRD peak intensities, peak locations and apparent fwhm values remain broadly consistent across water-immersion times. The two notable departures from this consistency are the stoichiometry of the O_2+UV treatment with no subsequent water immersion, and the specific BiOI-ascribable XRD reflections between the two types of treatment as shown in Fig. 3.1 vs Fig. 3.2.

A model consistent with the diffraction and photoelectron results includes distinct and unique mechanisms at work based on the respective oxidative conditions. Figure 4.1 presents a cartoon schematic for pathway-dependent oxidation. Instances in which immersion in degassed water oxidizes BiI_3(001) surfaces as in Fig. 4.1A, XP spectra remain consistent with the formation of BiOI for all 10–90 min immersion times under study while XRD traces strongly support the formation of BiOI(102) shown in Fig. 4.1B. While BiOI is well precedented as a water-driven oxidation product,[20] a specific observation of the (102) reflection of BiOI was unexpected in the context of it

not being the lowest-energy facet. However, Su and coworkers observed BiOI(102) reflections as the dominant XRD feature in direct hydrolyzation of BiI_3 nanopowders at elevated temperatures.[58] A possible rationale for our observation of the BiOI(102) reflection lies in structural similarities between that facet and BiI_3(001) layers. Figure 4.1B presents a [001] view of a hypothetical arrangement of a BiOI(102) adlayer above BiI_3(001) with superimposed bismuth atoms. In the instance of aligned bismuth atoms, iodine arrangements in BiOI(102) closely resemble atomic positions in BiI_3(001). While the unit cell spacing between BiOI(102) and BiI_3(001) are not completely commensurate, the similarities suggest that only nominal reorganization may be necessary for water-driven oxidation. Thus, we predict that the formation of BiOI(102) during oxidation in water may be guided by the high alignment in atomic registry between BiOI(102) and BiI_3(001). Future computational studies may further elucidate the adlayer structure of BiOI(102) on BiI_3(001), which may reveal additional insights into the water-driven oxidation dynamics. Notably, the longest oxidation time under study does present small quantities of BiOI(001) as shown in Figure 1D where several-nm thickness of the BiOI adlayer is no longer influenced by templating effects of the BiI_3 substrate and is rather driven by the formation of the lowest energy crystal face, BiOI(001). The present length scales complement longer term oxidation studies by Wagner et al. that principally observed BiOI(001) following several months of oxidation under humid air.[26]

In contrast to the water-driven oxidation of BiI_3 to BiOI, reactions driven by above-band-gap illumination under an oxygen ambient yields a strong suppression of I $3d_{5/2}$ photoelectron features that indicates oxide formation. The formation of a few-nm thick film of Bi_2O_3 is consistent with the photoelectron data in Fig. 3.3D, where the thickness of that film does not completely obscure contributions from the underlying BiI_3 substrate. Conversely, an incomplete suppression of the I $3d_{5/2}$ XPS feature may also result from the growth of an oxide layer with incomplete coverage that leaves BiI_3(001) regions exposed, or the conversion may yield bismuth oxyiodides of other stoichiometries such as Bi_5O_7I.[59] In each scenario, a thin oxide layer would be consistent with the absence of Bi_2O_3-ascribable or Bi_5O_7I-ascribable features in XRD traces as in Fig. 3.2A, which presents challenges for determining the crystallinity or exact composition of this oxidized layer. That the thickness of this oxidized layer remains smaller than a photoelectron sampling depth following two days of the O_2+UV treatment suggests that this oxidation may be self-passivating, or very slow. A slow oxidation rate complements observations of Hamdeh et alii observed where yellow films grew on BiI_3 following one week under illumination in a reaction they ascribed to the formation of bismuth oxides.[20] A lack of oxide-ascribable features in Fig. 3.2A does not necessarily preclude the possibility of a crystalline layer that may be too thin to yield diffraction features above the background. Investigations in to the crystallinity or amor-

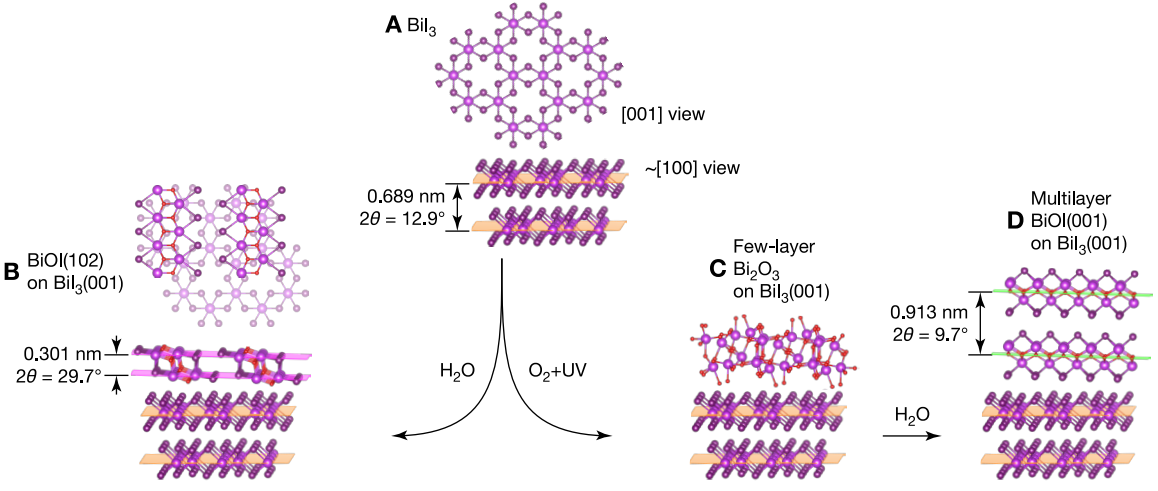

Figure 4.1 Proposed interfacial oxidation pathways from (A) freshly cleaved BiI_3 include (B) growth of BiOI(102) as a result of immersion in degassed water, or (C) growth of a thin layer of Bi_2O_3 as a result of UV irradiation under an oxygen ambient. Subsequent water immersion of a sample with a thin layer of Bi_2O_3 as in (C) yields (D) multilayer BiOI(001). Frames (A), (B), and (D) further include lattice layer spacing along with the corresponding experimentally observed Bragg angle (2θ).

phous nature of the interfacial oxide resulting from a O_2+UV treatment merit future study.

Subsequent water-driven oxidation of O_2+UV treated samples yields BiOI(001) instead of BiOI(102) that follows direct oxidization in water of tape-cleaved BiI_3(001). The observation of two different crystal faces of BiOI upon water-driven oxidation suggests a strong influence from the structure of the underlying substrate. For O_2+UV-treated samples with a thin layer of bismuth oxide, the growth of the low-energy, (001) facet of BiOI may be facilitated by a lack of atomic arrangement between the newly forming BiOI layer and the bismuth oxide on the substrate. This model of oxidation is further supported by the consistent observation of BiOI(001) inFig. 3.2B–D for successively longer immersions in water. Zhang et alii demonstrate the conversion of a surface layer of bismuth oxide to bismuth oxyiodide via water-driven iodide-capture in environmental contexts via chemisorption.[59] A chemisorption mechanism may be plausibly extended to the present water-driven conversion of interfacial oxides on BiI_3, considering that the water-only oxidation of BiI_3 to BiOI must liberate interfacial iodide species. Whether water intercalates between the BiI_3 and interfacial oxides or simply reacts at interfacial defects remains unclear from the present results, but the net result is BiOI(001) adlayers on BiI_3 whose orientation is strongly influenced by the interfacial oxide itself. In the case of a Bi_2O_3 interfacial oxide, its insolubility in neutral water precludes a possibility that water is simply dissolving the oxide prior to oxidizing the BiI_3,[60] which we would expect would have yielded BiOI(102) as observed in the water-only oxidation pathway.

Studies of oxidation reagents, products, and reaction pathways have important implications for the use of bismuth-based materials for solar energy conversion. Two aspects of the divergent oxidative pathways discussed above may be fertile arenas for future study relevant to photovoltaic device applications. Firstly, the predominance of distinct crystal faces observed in the two independent oxidative pathways likely correlates to different interfacial conditions between the substrate and its adlayer including surface defects. Future studies may be able to quantify the influence on carrier lifetimes, formation of trap-states, and other critical semiconductor parameters imposed by the particular interfacial characteristics resulting from these distinct oxidative mechanisms. Secondly, if the presence of ultrathin Bi_2O_3 on the substrate surface after O_2+UV exposure is indeed self-passivating or slow-growing, additional research is warranted to determine the relationship between oxide-based passivation of the underlying crystal substrate and the subsequent longevity of devices constructed of these materials. While a native oxide forms on the surface of crystalline silicon in approximately 24 h of ambient exposure,[61] many perovskite materials currently being evaluated for photovoltaic applications degrade in oxidizing conditions similar to those of our study in minutes.[46] The timescales established herein suggest that the

best pathway to minimal oxidation of BiI_3 materials lies in processing in the absence of water but may not necessitate oxygen-free environments.

CHAPTER 5

CONCLUSIONS AND FUTURE WORK

In vacuo vapor transport methods yielded single crystal BiI_3 that we subjected to a variety of oxidizing treatments. Oxidation due to immersion in degassed water yielded interfacial BiOI(102) of thicknesses of at least several nm following a 10 min immersion that grew in thickness with increasing immersion times. Oxidation due to exposure to above-bandgap UV illumination under an oxygen ambient yields oxidation that is consistent with an ultrathin layer of Bi_2O_3. Subsequent water immersion of the O_2+UV treated sample slowly converts the interfacial oxides to BiOI(001) over the course of several minutes. Future research on this material may focus on the evolution of the oxidative effects at shorter time scales as well as the role of step edge reactivity and passivation in preventing oxidation and maximizing environmental stability. While others have implicated some oxidation products as advantageous hole-blocking layers for BiI_3,[20] future studies should further correlate oxidation results to the carrier dynamics that are related to photovoltaics and other energy-conversion applications.

CHAPTER 6

REFERENCES

1. Dresselhaus, M. S.; Thomas, I. L., Alternative Energy Technologies. *Nature* **2001**, *414*, 332–337. 10.1038/35104599
2. Atwater, H. A.; Polman, A., Plasmonics for Improved Photovoltaic Devices. *Nat. Mater.* **2010**, *9*, 205–213. 10.1038/nmat2629
3. National Renewable Energy Laboratory. Best Research-Cell Efficiencies. (accessed 2 April 2022)
4. Babayigit, A.; Ethirajan, A.; Muller, M.; Conings, B., Toxicity of Organometal Halide Perovskite Solar Cells. *Nat. Mater.* **2016**, *15*, 247–251. 10.1038/nmat4572
5. Hao, F.; Stoumpos, C. C.; Cao, D. H.; Chang, R. P. H.; Kanatzidis, M. G., Lead-Free Solid-State Organic–Inorganic Halide Perovskite Solar Cells. *Nat. Photonics* **2014**, *8*, 489–494. 10.1038/nphoton.2014.82
6. Brandt, R. E., et al., Investigation of Bismuth Triiodide (BiI_3) for Photovoltaic Applications. *J. Phys. Chem. Lett.* **2015**, *6*, 4297–4302. 10.1021/acs.jpclett.5b02022
7. Kulkarni, A.; Singh, T.; Jena, A. K.; Pinpithak, P.; Ikegami, M.; Miyasaka, T., Vapor Annealing Controlled Crystal Growth and Photovoltaic Performance of Bismuth Triiodide Embedded in Mesostructured Configurations. *ACS Appl. Mater. Interfaces* **2018**, *10*, 9547–9554. 10.1021/acsami.8b00430
8. Möbs, J.; Gerhard, M.; Heine, J., $(HPy)_2(Py)CuBi_3I_{12}$, a Low Bandgap Metal Halide Photoconductor. *Dalton Trans.* **2020**, *49*, 14397–14400. 10.1039/D0DT03427D
9. Zhang, W.-B.; Xiang, L.-J.; Li, H.-B., Theoretical Perspective of Energy Harvesting Properties of Atomically Thin BiI_3. *J. Mater. Chem. A* **2016**, *4*, 19086–19094. 10.1039/C6TA06806E
10. Saito, T.; Iwasaki, T.; Kurosawa, S.; Yoshikawa, A.; Den, T., BiI_3 Single Crystal for Room-Temperature Gamma Ray Detectors. *Nucl. Instrum. Methods Phys. Res., Sect. A* **2016**, *806*, 395–400. 10.1016/j.nima.2015.10.036

11. Han, H.; Hong, M.; Gokhale, S. S.; Sinnott, S. B.; Jordan, K.; Baciak, J. E.; Nino, J. C., Defect Engineering of BiI_3 Single Crystals: Enhanced Electrical and Radiation Performance for Room Temperature Gamma-Ray Detection. *J. Phys. Chem. C* **2014**, *118*, 3244–3250. 10.1021/jp411201k

12. Gokhale, S. S.; Han, H.; Baciak, J. E.; Nino, J. C.; Jordan, K. A., Growth, Fabrication, and Testing of Bismuth Tri-Iodide Semiconductor Radiation Detectors. Radiat. Meas. **2015**, 74, 47–52. 10.1016/j.radmeas.2015.01.015

13. Johns, P. M.; Baciak, J. E.; Nino, J. C., Enhanced Gamma Ray Sensitivity in Bismuth Triiodide Sensors Through Volumetric Defect Control. *Appl. Phys. Lett.* **2016**, *109*, 092105. 10.1063/1.4962293

14. Lintereur, A. T.; Qiu, W.; Nino, J. C.; Baciak, J., Characterization of Bismuth Tri-Iodide Single Crystals for Wide Band-Gap Semiconductor Radiation Detectors. *Nucl. Instrum. Methods Phys. Res., Sect. A* **2011**, *652*, 166–169. 10.1016/j.nima.2010.12.013

15. Matsumoto, M.; Hitomi, K.; Shoji, T.; Hiratate, Y., Bismuth Tri-Iodide Crystal for Nuclear Radiation Detectors. *IEEE Trans. Nucl. Sci.* **2002**, *49*, 2517–2520. doi.org/10.1109/TNS.2002.803883

16. Fornaro, L.; Cuna, A.; Noguera, A.; Perez, M.; Mussio, L. In *Growth of Bismuth Tri-Iodide Platelets for Room Temperature X-Ray Detection*, 2003 IEEE Nuclear Science Symposium. Conference Record (IEEE Cat. No.03CH37515), 19-25 Oct. **2003**, *5*, pp 3541–3544. 10.1109/NSSMIC.2003.1352675

17. Dmitriyev, Y.; Bennett, P.; Cirignano, L.; Klugerman, M.; Shah, K., Bismuth Iodide Crystals as a Detector Material: Some Optical and Electrical Properties. In *Hard X-Ray, Gamma-Ray, and Neutron Detector Physics*, Proc. SPIE 3768, Hard X-Ray, Gamma-Ray, and Neutron Detector Physics: 1999. 10.1117/12.366625

18. Liu, Y.; Sun, H.; Yang, D.; Wangyang, P.; Gao, X.; Gou, Z.; Zhu, X., Electrical Properties of X-Ray Detector Based on Bismuth Tri-Iodide Single Crystal with Electrode Configuration Considering. *Mater. Res. Express* **2019**, *6*, 055902. 10.1088/2053-1591/aaff87

19. Bremner, S. P.; Levy, M. Y.; Honsberg, C. B., Analysis of Tandem Solar Cell Efficiencies Under AM1.5G Spectrum Using a Rapid Flux Calculation Method. *Prog. Photovoltaics* **2008**, *16*, 225-233. 10.1002/pip.799

20. Hamdeh, U. H.; Nelson, R. D.; Ryan, B. J.; Bhattacharjee, U.; Petrich, J. W.; Panthani, M. G., Solution-Processed BiI_3 Thin Films for Photovoltaic Applications: Improved Carrier Collection via Solvent Annealing. *Chem. Mater.* **2016**, *28*, 6567–6574. 10.1021/acs.chemmater.6b02347

21. Boopathi, K. M.; Raman, S.; Mohanraman, R.; Chou, F.-C.; Chen, Y.-Y.; Lee, C.-H.; Chang, F.-C.; Chu, C.-W., Solution-Processable Bismuth Iodide Nanosheets as Hole Transport Layers for Organic Solar Cells. *Sol. Energy Mater. Sol. Cells* **2014**, *121*, 35–41. 10.1016/j.solmat.2013.10.031

22. Yoo, B.; Ding, D.; Marin-Beloqui, J. M.; Lanzetta, L.; Bu, X.; Rath, T.; Haque, S. A., Improved Charge Separation and Photovoltaic Performance of BiI_3 Absorber Layers by Use of an In Situ Formed BiSI Interlayer. *ACS Appl. Energy Mater.* **2019**, *2*, 7056–7061. 10.1021/acsaem.9b00838

23. Komatsu, T.; Karasawa, T.; Jida, T.; Miyata, K.; Kaifu, Y., Secondary Emission of Indirect Exciton in BiI_3. *J. Lumin.* **1981**, *24/25*, 679–682. 10.1016/0022-2313(81)90069-7

24. Masroor, M.; Yan, T.; McRae, J.; Molstad, E.; Rivas, R.; Ruano, E.; McClelland, A.; Rao, P., Controlling Crystal Growth of Non-Toxic Bismuth Iodide (BiI_3) Semiconducting Material for Efficient Photovoltaics; *SPIE*, **2020**; Vol. 11275. 10.1117/12.2544043

25. Podraza, N. J.; Qiu, W.; Hinojosa, B. B.; Xu, H.; Motyka, M. A.; Phillpot, S. R.; Baciak, J. E.; Trolier-McKinstry, S.; Nino, J. C., Band Gap and Structure of Single Crystal BiI_3: Resolving Discrepancies in Literature. *J. Appl. Phys.* **2013**, *114*, 033110. 10.1063/1.4813486

26. Wagner, B.; Huttner, A.; Bischof, D.; Engel, A.; Witte, G.; Heine, J., Chemical Surface Reactivity and Morphological Changes of Bismuth Triiodide (BiI_3) under Different Environmental Conditions. *Langmuir* **2020**, *36*, 6458–6464. 10.1021/acs.langmuir.0c00740

27. Lehner, A. J.; Wang, H.; Fabini, D. H.; Liman, C. D.; Hábert, C.-A.; Perry, E. E.; Wang, M.; Bazan, G. C.; Chabinyc, M. L.; Seshadri, R., Electronic Structure and Photovoltaic Application of BiI_3. *Appl. Phys. Lett.* **2015**, *107*, 131109. 10.1063/1.4932129

28. Wei, Q.; Chen, J.; Ding, P.; Shen, B.; Yin, J.; Xu, F.; Xia, Y.; Liu, Z., Synthesis of Easily Transferred 2D Layered BiI_3 Nanoplates for Flexible Visible-Light Photodetectors. *ACS Appl. Mater. Interfaces* **2018**, *10*, 21527–21533. 10.1021/acsami.8b02582

29. Diaz-Torres, L. A.; Gomez-Solis, C.; Oliva, J.; Coutino-Gonzalez, E., Highly Efficient Hydrogen Generation of BiI_3 Nanoplates Decorated with Ag Nanoparticles. *Int. J. Hydrogen Energy* **2018**, *43*, 15962–15974. 10.1016/j.ijhydene.2018.06.182

30. Li, J.; Guan, X.; Wang, C.; Cheng, H.-C.; Ai, R.; Yao, K.; Chen, P.; Zhang, Z.; Duan, X.; Duan, X., Synthesis of 2D Layered BiI_3 Nanoplates, BiI_3/WSe_2 van der Waals Heterostructures and Their Electronic, Optoelectronic Properties. *Small* **2017**, *13*, 1701034. 10.1002/smll.201701034

31. Ashokkumar, A. E.; Enyashin, A. N.; Deepak, F. L., Single Walled BiI_3 Nanotubes Encapsulated within Carbon Nanotubes. *Sci. Rep.* **2018**, *8*, 10133. 10.1038/s41598-018-28446-2

32. Achoi, M. F.; Noman, M. A. A.; Kato, S.; Kishi, N.; Soga, T., Synthesis of Bismuth Triiodide Nanofibers by Spin-Coating at Room Temperature. *Materialia* **2021**, *16*, 101077. 10.1016/j.mtla.2021.101077

33. Zhu, Y.; Zhang, Q.; Kam, M.; Poddar, S.; Gu, L.; Liang, S.; Qi, P.; Miao, F.; Fan, Z., Vapor Phase Fabrication of Three-Dimensional Arrayed BiI_3 Nanosheets for Cost-Effective Solar Cells. *InfoMat* **2020**, *2*, 975–983. 10.1002/inf2.12070

34. Aguiar, I.; Kröger, S.; Fornaro, L., Bismuth Tri-Iodide Polycrystalline Films for X-ray Direct and Digital Imagers. *Nucl. Instrum. Methods Phys. Res., Sect. A* **2009**, *610*, 332–334. 10.1016/j.nima.2009.05.184

35. Nason, D.; Keller, L., The Growth and Crystallography of Bismuth Tri-Iodide Crystals Grown by Vapor Transport. *J. Cryst. Growth* **1995**, *156*, 221–226. 10.1016/0022-0248(95)00291-X

36. Sun, H.; Zhu, X.; Wangyang, P.; Gao, X.; Zhu, S.; Zhao, B., Preparation and Characterization of Free-Standing BiI_3 Single-Crystal Flakes for X-Ray Detection Application. *J. Mater. Sci.: Mater. Electron.* **2018**, **29**, 20003–20009. 10.1007/s10854-018-0130-x

37. Wang, Y.; Shi, X.; Wang, G.; Tong, J.; Pan, D., All-Inorganic and Lead-Free BiI_3 Thin Film Solar Cells by Iodization of BiSI Thin Films. *J. Mater. Chem. C* **2020**, *8*, 14066–14074. 10.1039/D0TC03753B

38. Cho, S. B.; Gazquez, J.; Huang, X.; Myung, Y.; Banerjee, P.; Mishra, R., Intrinsic Point Defects and Intergrowths in Layered Bismuth Triiodide. *Phys. Rev. Mater.* **2018**, *2*, 064602. 10.1103/PhysRevMaterials.2.064602

39. Christians, J. A.; Miranda Herrera, P. A.; Kamat, P. V., Transformation of the Excited State and Photovoltaic Efficiency of $CH_3NH_3PbI_3$ Perovskite upon Controlled Exposure to Humidified Air. *J. Am. Chem. Soc.* **2015**, *137*, 1530–1538. 10.1021/ja511132a

40. Yan, H.; Ziyu, H.; Xu, G.; Xiaohong, S., Structural, Electronic and Photocatalytic Properties of Atomic Defective BiI_3 Monolayers. *Chem. Phys. Lett.* **2018**, *691*, 341–346. 10.1016/j.cplett.2017.11.044

41. Muir, M. M. P.; Hoffmeister, G. B.; Robbs, C. E., IV. Contributions from the Laboratory of Gonville and Caius College, Cambridge. No. VII. On Bismuth and Bismuth Compounds. *J. Chem. Soc., Trans.* **1881**, *39*, 21–37. 10.1039/CT8813900021

42. Zeng, W.; Li, J.; Feng, L.; Pan, H.; Zhang, X.; Sun, H.; Liu, Z., Synthesis of Large-Area Atomically Thin BiOI Crystals with Highly Sensitive and Controllable Photodetection. *Adv. Funct. Mater.* **2019**, *29*, 1900129. 10.1002/adfm.201900129

43. Martin, J. L.; Stoflet, R.; Carl, A. D.; Himmelberger, K. M.; Granados-Fócil, S.; Grimm, R. L., Quantification of Surface Reactivity and Step-Selective Etching Chemistry on Single-Crystal BiOI(001). *Langmuir* **2020**, *36*, 9343–9355. 10.1021/acs.langmuir.0c00980

44. Mendes, J. L.; Gao, W.; Martin, J. L.; Carl, A. D.; Deskins, N. A.; Granados-Focil, S.; Grimm, R. L., Interfacial States, Energetics, and Atmospheric Stability of Large-Grain Antifluorite Cs_2TiBr_6. *J. Phys. Chem. C* **2020**, *124*, 24289–24297. 10.1021/acs.jpcc.0c08719

45. Liu, H.; Cai, J.; Luo, M.; Chen, C.; Hu, P., Novel Mesoporous Bismuth Oxyiodide Single-Crystal Nanosheets with Enhanced Catalytic Activity. *RSC Adv.* **2020**, *10*, 5913–5918. 10.1039/C9RA10451H

46. Bryant, D.; Aristidou, N.; Pont, S.; Sanchez-Molina, I.; Chotchunangatchaval, T.; Wheeler, S.; Durrant, J. R.; Haque, S. A., Light and Oxygen Induced Degradation Limits the Operational Stability of Methylammonium Lead Triiodide Perovskite Solar Cells. *Energy Environ. Sci.* **2016**, *9*, 1655–1660. 10.1039/C6EE00409A

47. Cullity, B. D., Elements of X-ray Diffraction, 2nd ed.; Addison-Wesley Publishing Company, 1978. ISBN 9781295806829

48. Garg, A.; Tomar, M.; Gupta, V., Synthesis and Characterisation of Thin Films of Bismuth Triiodide for Semiconductor Radiation Detectors. *Conf. Pap. Sci. 2014*, **2014**, 370436. 10.1155/2014/370436

49. Olivero, J. J.; Longbothum, R. L., Empirical Fits to the Voigt Line Width: A Brief Review. *J. Quant. Spectrosc. Radiat. Transfer* **1977**, *17*, 233–236. 10.1016/0022-4073(77)90161-3

50. Carl, A. D.; Kalan, R. E.; Obayemi, J. D.; Zebaze Kana, M. G.; Soboyejo, W. O.; Grimm, R. L., Synthesis and Characterization of Alkylamine-Functionalized Si(111) for Perovskite Adhesion With Minimal Interfacial Oxidation or Electronic Defects. *ACS Appl. Mater. Interfaces* **2017**, *9*, 34377–34388. 10.1021/acsami.7b07117

51. Fairley, N. Peak Fitting in XPS. (accessed August 2015).

52. Moulder, J. F.; Stickle, W. F.; Sobol, P. E.; Bomben, K. D., Handbook of X-ray Photoelectron Spectroscopy; Physical Electronics Division: Perkin-Elmer Corporation, 1992.

53. Shirley, D. A., High-Resolution X-Ray Photoemission Spectrum of the Valence Bands of Gold. *Phys. Rev. B* **1972**, *5*, 4709–4714. 10.1103/PhysRevB.5.4709

54. Tougaard, S., Formalism for Quantitative Surface Analysis by Electron Spectroscopy. *J. Vac. Sci. Technol., A* **1990**, *8*, 2197–2203. 10.1116/1.577037

55. Jansson, C.; Hansen, H. S.; Yubero, F.; Tougaard, S., Accuracy of the Tougaard Method for Quantitative Surface Analysis. Comparison of the Universal and REELS Inelastic Cross Sections. *J. Electron Spectrosc. Relat. Phenom.* **1992**, *60*, 301–319. 10.1016/0368-2048(92)80025-4

56. Dresselhaus, M. S.; Dresselhaus, G., Intercalation Compounds of Graphite. *Adv. Phys. 2002*, *51*, 1–186. 10.1080/00018730110113644

57. Motter, J. P.; Koski, K. J.; Cui, Y., General Strategy for Zero-Valent Intercalation into Two-Dimensional Layered Nanomaterials. *Chem. Mater.* **2014**, *26*, 2313–2317. 10.1021/cm500242h

58. Su, J.; Xiao, Y.; Ren, M., Direct Hydrolysis Synthesis of BiOI Flowerlike Hierarchical Structures and Its Photocatalytic Activity under Simulated Sunlight Irradiation. *Catal. Commun.* **2014**, *45*, 30–33. 10.1016/j.catcom.2013.10.020

59. Zhang, L.; Gonçalves, A.; Jiang, B.; Jaroniec, M., Capture of Iodide by $BiVO_4$ and Bi_2O_3: An Insightful Look at the Process and its Aftermath. *ChemSusChem* **2018**, *11*, 1486–1493. 10.1002/cssc.201800327

60. Cotton, A. F.; Wilkinson, G.; Murillo, C. A.; Bochmann, M., Advanced Inorganic Chemistry, 6th ed.; Wiley, 1999. ISBN 9780471199571

61. Morita, M.; Ohmi, T., Characterization and Control of Native Oxide on Silicon. *Jpn. J. Appl. Phys.* **1994**, *33*, 370–374. 10.1143/jjap.33.370